Characterization of Die-Swell in Thermoplastic Material Extrusion

Austin R. Colon[a,b], David O. Kazmer[a], Amy M. Peterson[a], Jonathan E. Seppala[b,*]

[a]Department of Plastics Engineering, University of Massachusetts Lowell, Lowell, Massachusetts 01854 USA
[b]Materials Science and Engineering Division, National Institute of Standards and Technology, Gaithersburg, MD 20899 USA

*Corresponding Author:
Jonathan E. Seppala
National Institute of Standards and Technology
100 Bureau Dr.
Gaithersburg, MD 20899-8542, USA
Email: jonathan.seppala@nist.gov
Phone: (301) 975-2836

Highlights

- Simultaneous measurement of extrudate shape, temperature, and infeed pressure.
- Swell ratio correlates with infeed pressure as a function of flow rate, hot end temperature, and nozzle orifice diameter.
- Swell ratio correlates with shear stress and is modeled using Tanner's equation.
- Tanner's constant increases as a function of hot end temperature.
- Tanner's constant correlates with inverse of zero-shear viscosity as a function of temperature.

Abstract

Die-swell is a flow effect that occurs in polymer extrusion whereby the material experiences rapid stress and dimensional changes upon exiting the nozzle orifice. Material extrusion additive manufacturing is no exception, and this effect influences the final dimensions of the printed road and imparts residual stresses. Die-swell is measured via a custom test cell that uses optical and infrared cameras and an instrumented hot end with an infeed pressure load cell. The instrumented hot end is mounted onto a stationary extruder above a conveyor to simulate printhead translation at steady state conditions for a wide range of volumetric flow rates. Investigated factors for an acrylonitrile butadiene styrene (ABS) filament include volumetric

flow rate (0.9 mm^3/s to 10.0 mm^3/s), hot end temperature setpoint (200 °C to 250 °C), and nozzle orifice diameter (0.25 mm to 0.60 mm). The die-swell increases as a function of the volumetric flow rate and shear stress but decreases as a function of the hot end temperature setpoint and nozzle orifice diameter. For modelling, an implementation of the Tanner model for die-swell displays good agreement with experimental results. The model also demonstrates that the same proportionality constant, k_{N_1}, which relates first normal stress difference to shear stress, can be used for different nozzle orifice diameters with the same length to diameter ratios, and that k_{N_1} increases as a function of hot end temperature setpoint as expected with the rheological concept of time temperature superposition.

Keywords
Material extrusion
Die-swell
Fused deposition modeling (FDM)
Instrumentation
Rheology

1. Introduction

The thermoplastic material extrusion process is capable of producing complex geometries [1] for a wide variety of materials with a simple filament feedstock [2]. Material extrusion is used in a variety of applications, ranging from medical models [3] to prototyping injection mold inserts [4]. Limitations to further adoption of material extrusion include anisotropic mechanical properties [5-8], variable feedstock quality (due to varying composition) [9-12], and the sensitivity of final part quality (e.g., dimensional accuracy, surface roughness, mechancial properties) to process parameters [13, 14].

In filament-based material extrusion, the feedstock, in filament form, is heated to create a melt and driven through the orifice of a nozzle to form the roads that comprise a part. When the material is driven through the nozzle orifice, as shown in Figure 1, the melt deforms, resulting in

stresses that cause the material to expand upon exit. This pheonomenon, known as die-swell, is present in both Newtonian and non-Newtonian materials [15-17]. It has been widely studied in other polymer extrusion processes, such as capillary rheology and single-screw extrusion [16, 18-26]. In these works, die-swell was found to vary as a function of melt temperature, die design, volumetric flow rate, and shear stress [18, 20, 21]; it is expected to be most observable at high volumetric flow rates and shear stresses and low melt temperatures and die length to diameter ratios. Researchers have sought to model die-swell [16, 27-30] because it influences final product properties and requires process troubleshooting to mitigate the resulting geometric distortion [20, 24].

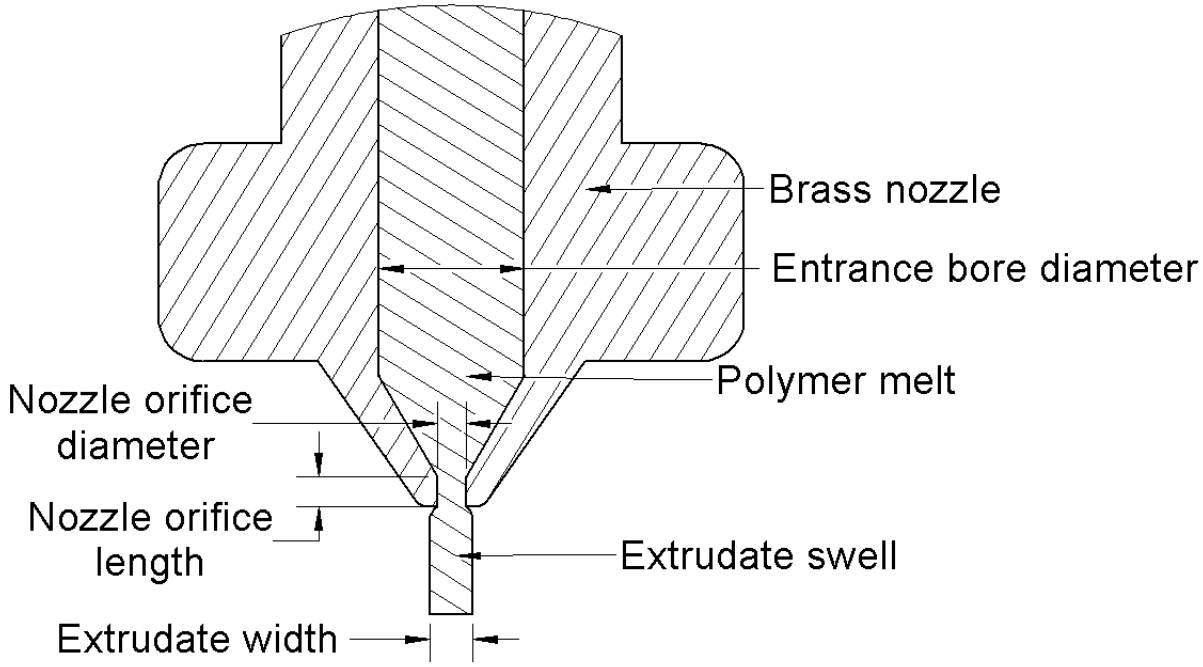

Figure 1: An E3D V6 material extrusion nozzle and the die-swell phenomenon. Significant dimensions of the nozzle are called out and will be referenced in the analysis.

Material extrusion is also prone to die-swell, so it should be considered in process parameter selection to ensure acceptable parts [31, 32]. Other rheological effects observed in

material extrusion that could combine with die-swell to affect part quality include material compressibility [33] and contact pressures [34]. One example of die-swell's effects is that it influences the orientation of short fibers, leading to further anisotropy in mechanical properties of chopped fiber-filled material extrusion parts [35]. Die-swell can also lead to road widths varying from their specified dimensions [36-38].

Optical cameras can be used to image the extrudate when studying die-swell at steady state in extrusion processes [38, 39], with the cameras typically placed perpendicular to the flow direction [39]. Rotational rheology may be performed on the feedstock to characterize the viscoelastic properties of the material. This rheology information is valuable because the first normal stress difference can be correlated with degree of swell according to Tanner [16]. In material extrusion, other researchers have used infeed force or pressure measurements [37, 40, 41], optical cameras [37, 38, 41-47], and infrared (IR) cameras [37, 41, 47-55] to study the behavior of extrudate exiting the nozzle. Techniques to observe die-swell, and polymer flow in general, range from measuring the extrudate during steady extrusion over the print bed to using novel experimental apparati [37, 42] to observe the melt as it advances through a glass pipette capillary [45]. In previous material extrusion studies, IR temperature measurements were not correlated with the observed die-swell [37]. Both numerical and analytical models are discussed in the literature [42, 56-59].

When designing a new system to quantify die-swell, in-situ pressure measurements are especially attractive because they allow for estimation of rheological properties and stresses as the polymer flows through the nozzle. Optical imaging is critical for measuring the extrudate's dimensions. IR thermography is also desirable because polymer flow behavior varies as a function of both temperature and flow rate, and it is expected that melt temperature affects the

magnitude of die-swell. Many other sensing techniques could also be employed to estimate the process condition, but the three mentioned (infeed force, optical imaging, and IR thermography) were the focus of literature review for die-swell since they provide information about the process with minimal interference.

For this work, the authors' goal is to employ a system for measuring die-swell that is capable of continuous, dynamic data collection for the material extrusion process. This was accomplished by building a test cell with a material extrusion printhead, possessing an infeed pressure sensor, above a conveyor. An optical camera is oriented along the print direction of the conveyor and an IR camera is aligned perpendicular to the print direction. This setup shows promise for measuring the die-swell of thermoplastic-based filaments, and for correlating die-swell with various process factors and responses, as demonstrated by the described results.

With offline characterization via a capillary rheometer, the die-swell ratio also shows the expected increasing trend with shear stress in the nozzle orifice. The Tanner model for die-swell was fit to the measurements to predict swell as a function of the shear stress experienced in the nozzle orifice. Good model fits are shown and the proportionality constant, relating the first normal stress difference to the shear stress, is observed to increase as a function of temperature and be constant across nozzle orifice diameters of the same length to diameter ratio and entrance bore diameter. In addition to these insights, the implemented system shows the potential for characterizing variable feedstocks, studying the material extrusion process further, and provides data for process model validation.

2. Materials and methods[1]

2.1. Feedstock & characterization

The material of focus for this work is acrylonitrile butadiene styrene (Hatchbox ABS, black, 1.75 mm diameter) with a recommended processing temperature range of 210 °C to 240 °C. ABS was chosen based on its popularity in the material extrusion market, its use in other studies focusing on die-swell, and preliminary experiments where it showed the highest degree of die-swell [37, 45, 58, 60]. The filament was purchased from Hatchbox (Pomona, CA) and used as received. Capillary rheology at three different temperatures and ten shear rates was performed in accordance with ASTM D3835 – 16 on a Dynisco (Franklin, MA) LCR7000 capillary rheometer. Two dies with length to diameter ratios of 10:1 and 30:1 were used. A Cross model with the Williams-Landel-Ferry (WLF) temperature dependance (Cross-WLF) [61] was fit to the data, after the Bagley correction. The Cross model is of the form:

$$\eta(\dot{\gamma}, T) = \eta_0/(1 + (\eta_0\dot{\gamma}/\tau^*)^{1-n}) \quad (1)$$

where η is the shear viscosity, $\dot{\gamma}$ is the shear rate, T is the temperature, τ^* is the critical shear stress, n is the power-law index, and η_0 is the zero-shear viscosity defined as:

$$\eta_0 = \eta_{ref}\exp(-(A_1(T - T_{ref}))/(A_2 + T - T_{ref})) \quad (2)$$

η_{ref} is the reference temperature viscosity, T_{ref} is the glass transition temperature, and A_1 and A_2 are coefficients that are fit to capture the temperature dependency of the viscosity. The fitted coefficients for the Cross-WLF model are shown in Table 1.

[1] Certain commercial equipment, instruments, or materials are identified in this paper in order to specify the experimental procedure adequately. Such identification is not intended to imply recommendation or endorsement by the National Institute of Standards and Technology, nor is it intended to imply that the materials or equipment identified are necessarily the best available for the purpose.

Table 1: Cross-WLF model coefficients for black ABS filament.

Coefficient	Value
n	0.341
τ^* [Pa]	41070
η_{ref} [Pa-s]	2.54 x 10^{12}
T_{ref} [K]	365
A_1	28.3
A_2 [K]	51.6

To calculate the viscosity, isothermal tube flow was assumed, and the material was assumed to be shear thinning. To account for shear thinning, the shear rate is calculated with the Weissenberg-Rabinowitsch corrected formula:

$$\dot{\gamma}_w = \dot{\gamma}_{aw}(1/4)(3 + (1/n)) \quad (3)$$

where $\dot{\gamma}_w$ is the shear rate at the wall and $\dot{\gamma}_{aw}$ is the apparent shear rate at the wall, defined as:

$$\dot{\gamma}_{aw} = 4Q/\pi r^3 \quad (4)$$

In this formula, Q is the volumetric flow rate and r is the radius of the tube, which in this case is the nozzle orifice. The shear viscosity shown in Figure 2 was calculated with the Weissenberg-Rabinowitsch-corrected shear rate at the wall and demonstrates the shear thinning behavior of ABS. As expected, the viscosity decreases as a function of the temperature. The shear stress was calculated according to Newton's law of viscosity:

$$\tau = \mu\dot{\gamma} \quad (5)$$

where τ is the shear stress at the wall and μ is the dynamic viscosity calculated as the Cross-WLF shear viscosity. The shear stress as a function of the shear rate is shown in Figure 2 and exhibits an increase in shear stress with shear rate.

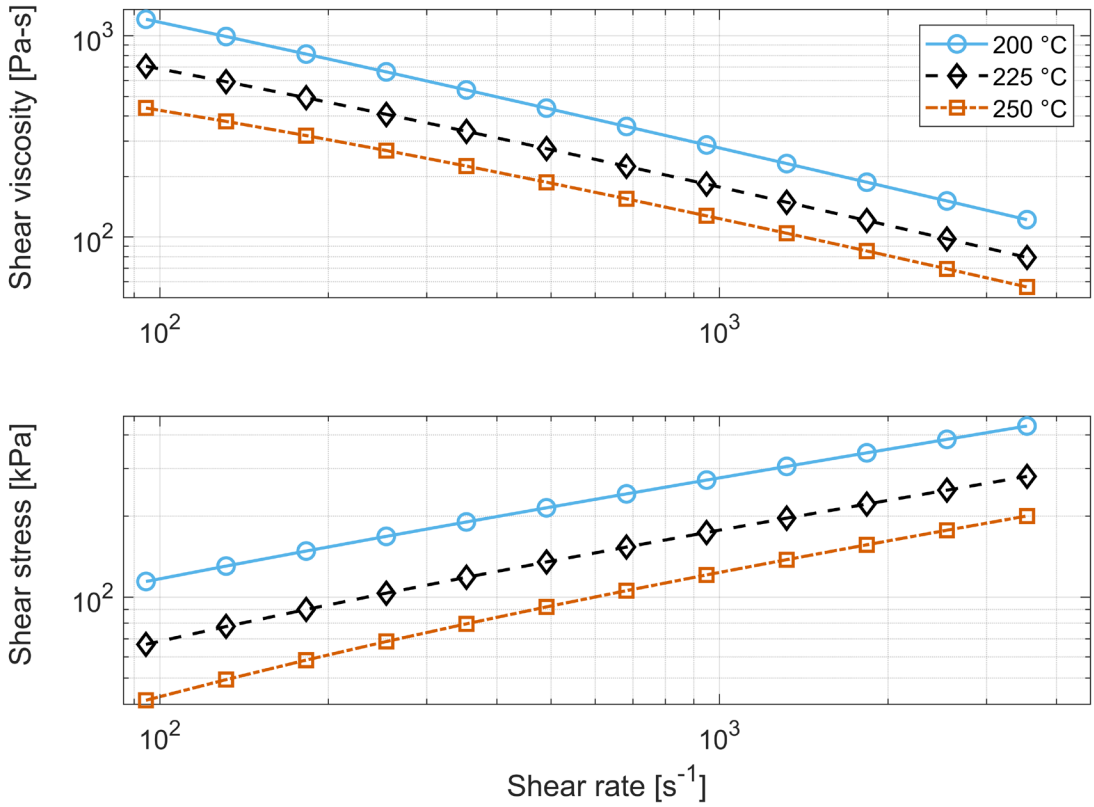

Figure 2: Log-Log plots of shear viscosity (top) and shear stress (bottom) as a function of shear rate for the ABS filament used in this study. The temperatures and shear rates used are reflective of experimental conditions and are representative of the temperatures and shear rates observed in the material extrusion printer.

2.2. Measurement system design

For this system, a custom bronze hot end with 1.75 mm diameter filament was used (see Figure 3). The design is intended to enhance melting capacity via a lofted transition from a circular flow bore to a rectangular slit, and back again. The two heater cartridges increase melting capacity compared to most hot ends that possess one heater. A 100 kΩ thermistor was used to monitor and control the temperature of the hot end. The hot end design was manufactured in bronze by i.Materialise (Leuven, Belgium) via a casting process. The stainless-

steel heat break is the standard version used on Creality (Shenzhen, China) material extrusion 3D printers. The polytetrafluoroethylene (PTFE) tube (2 mm and 4 mm inner and outer diameter, respectively) was purchased through Filastruder (Snellville, GA). Lastly, the brass nozzles are a V6 model purchased from McMaster-Carr (Santa Fe Springs, CA) with a M6 thread, intended for use with 1.75 mm diameter filament.

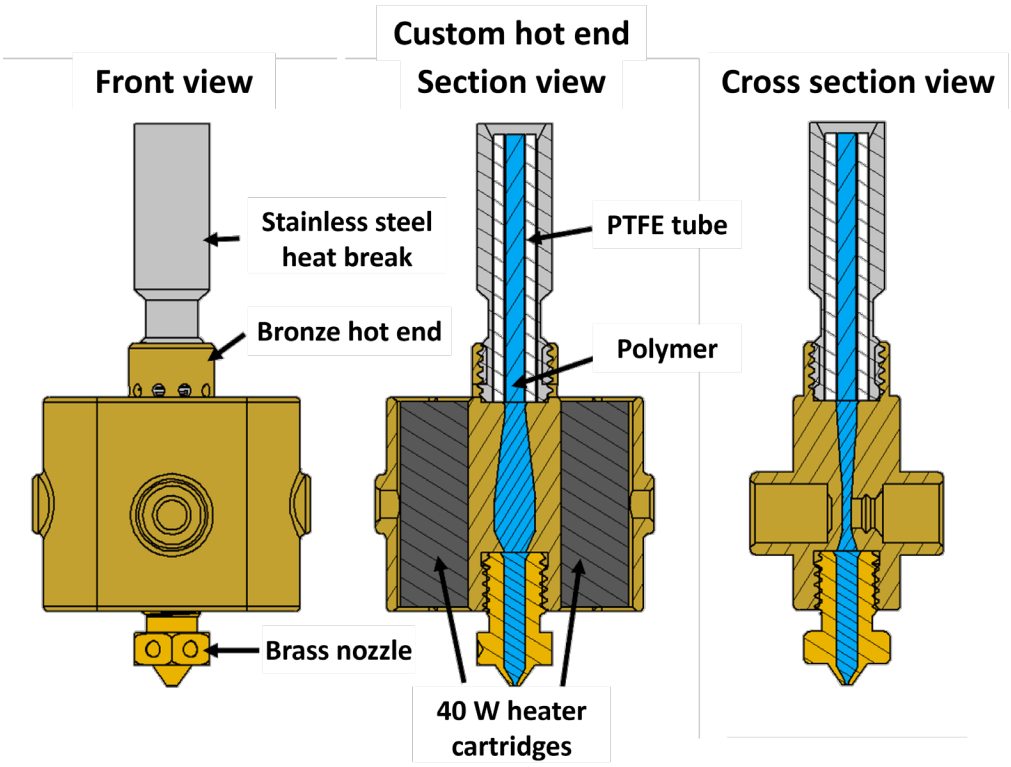

Figure 3: The custom hot end used in the measurement system.

Brass nozzles were purchased with three different nozzle orifice diameters. These diameters were selected based on common use in systems and with the intent of generating observable changes in the degree of die-swell. A 0.40 mm nozzle is commonly used on desktop printers. According to the drawings from McMaster-Carr, these nozzles all have nozzle orifice lengths equal to their nozzle orifice diameters, giving them all length to diameter ratios of one.

Since all brass nozzles have the same entrance bore diameter (see Figure 1), a contraction ratio was calculated to estimate the expected degree of die-swell that would be observed for each nozzle, since die-swell is attributed to the elastic memory of the polymer. The contraction ratio, $R_{contraction}$, was calculated as:

$$R_{contraction} = A_{EB}/A_O \quad (6)$$

wherein

$$A_{EB} = \pi {r_{EB}}^2 \quad (7)$$

where $r_{EB}$is the radius of the entrance bore of the nozzle, and A_O is the area of the orifice region of the nozzle flow bore:

$$A_O = \pi {r_O}^2 \quad (8)$$

where r_O is the radius of the orifice. The contraction ratios for all three of the nozzles used in this work are shown in Table 2. The 0.25 mm nozzle has the greatest contraction ratio and would be expected to demonstrate the highest degree of die-swell, while the 0.60 mm nozzle has the lowest contraction ratio and should demonstrate the lowest degree of die-swell.

Table 2: Material extrusion nozzle orifice diameters and their contraction ratios.

Nozzle orifice diameter [mm]	**Contraction ratio**
0.25	64
0.40	25
0.60	11

The implemented system, including the hot end, is shown in Figure 4. The hot end is mounted to a 5 kg beam-style load cell from Sparkfun (Niwot, CO, Part Number: SEN-14729, combined error of 0.05 % of the full-scale value) to measure the infeed pressure. The load cell is mounted to a custom aluminum instrumentation plate, which is attached to a Micro-Swiss

(Ramsey, MN) direct drive extruder, intended for a Creality Ender 5, with a standard Creality 42-40 (NEMA 17) stepper motor and heat sink. The extruder is mounted on an XY linear stage from Newport (Irvine, CA, model no. 401) with a high load precision lab jack (Newport model no. 281). The XY stage allows focusing of the nozzle and extrudate in the optical camera's view and positioning the nozzle over the conveyor belt, while the high load precision lab jack enables adjustment of the height between the bottom face of the brass nozzle and the top of the conveyor belt. The height between the nozzle and the conveyor was maintained at 4 mm during the reported experiments to allow for videography of the swelling extrudate.

The conveyor is a custom design manufactured for this system and is intended to continuously remove the extrudate from below the nozzle. It consists of a 22 cm (9.0 inch) inner circumference and 6.3 mm (0.25 inch) wide rubber belt from Elliot Electronic Supply (Tucson, AZ), two aluminum pulleys (one driven by a Creality 42-40 stepper motor and a follower), a nylatron platform (also capable of functioning as a vacuum chuck) to stabilize the belt under the load of the extruder (manufactured in-house), and an aluminum frame (manufactured in-house). The conveyor is also mounted on a high load precision lab jack from Newport (model no. 271) to allow positioning relative to the nozzle.

The conveyor and extruder stepper motors, along with the hot end heaters, are controlled via a Creality motherboard (model no: V4.2.7) and liquid crystal display (LCD) screen. The firmware on the motherboard is a modified version of Marlin 2.0 configured for a Creality Ender 5 Pro. This version of the firmware was modified to remove the y-axis limit (to enable continuous rotation of the conveyor stepper) and increase the maximum hot end temperature. Programmed Gcode instructions are loaded onto the motherboard via a microSD card.

The optical and IR cameras focus on the extrudate as it exits the nozzle orifice, with the primary light source positioned opposite the optical camera for backlighting the extrudate images. The optical camera is from Basler (Highland, IL, model no. acA1920-50gc) with a resolution of 1920 x 1200 pixels, and an objective zoom from Leica (Teaneck, NJ, model no. Z16-APO). The IR camera is from FLIR (Wilsonville, OR, model no. A6701sc) with a resolution of 640 x 512 pixels, 50 mm lens, 19.05 mm extender ring, and a spectral range of 3.0 µm to 5.0 µm. The spectral range is further limited with a 3900 nm notch filter with 400 nm bandwidth (Spectragon BP-3900-200 nm). Both cameras are set to record at 30 Hz. For the optical camera, the aperture is closed on the objective zoom, which is set to 4x, and the backlight is kept at its minimum setting. The exposure time is set to 20,000 µs and the gain is set to zero on the Pylon Viewer software for the optical camera. In ResearchIR, the control software for the IR camera, a 0.60 ms integration time is set.

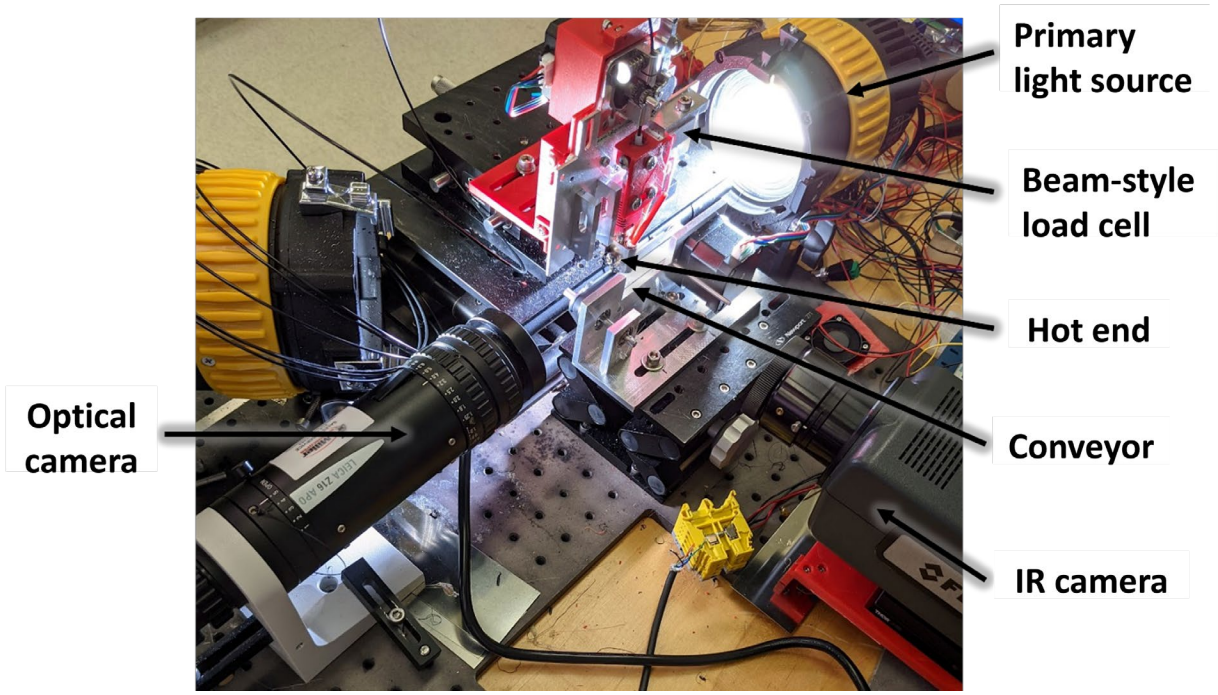

Figure 4: The measurement system.

2.3. Data acquisition & processing

For data acquisition, three pieces of software are utilized. The first is MATLAB (Mathworks, Natick, MA), followed by Pylon Viewer and ResearchIR. To initiate data acquisition, the cameras are set in Pylon Viewer and ResearchIR to await an analog synchronization signal. After the camera configurations are verified, the recording sessions are started for the cameras. A MATLAB script that configures the data acquisition of the analog signal for the load cell is used to configure a pulse width modulated sync signal for 30 Hz. Once the MATLAB script is run, the cameras start recording frames and the data acquisition system (DAQ), a National Instruments (Austin, TX) USB 6212 (BNC), collects analog data. A sampling frequency of 50 kHz with buffering frequency of 250 Hz gather data from the load cell. It should be noted that the signal for the load cell passes through an OMEGA (Norwalk, CT, model no. DRF-LC) strain gauge signal amplifier configured to accept 0 mV to 20 mV and output a range of 0 V to 10 V. An excitation voltage of 10 V is supplied to the load cell. The flow of data for this acquisition system is shown in Figure 5.

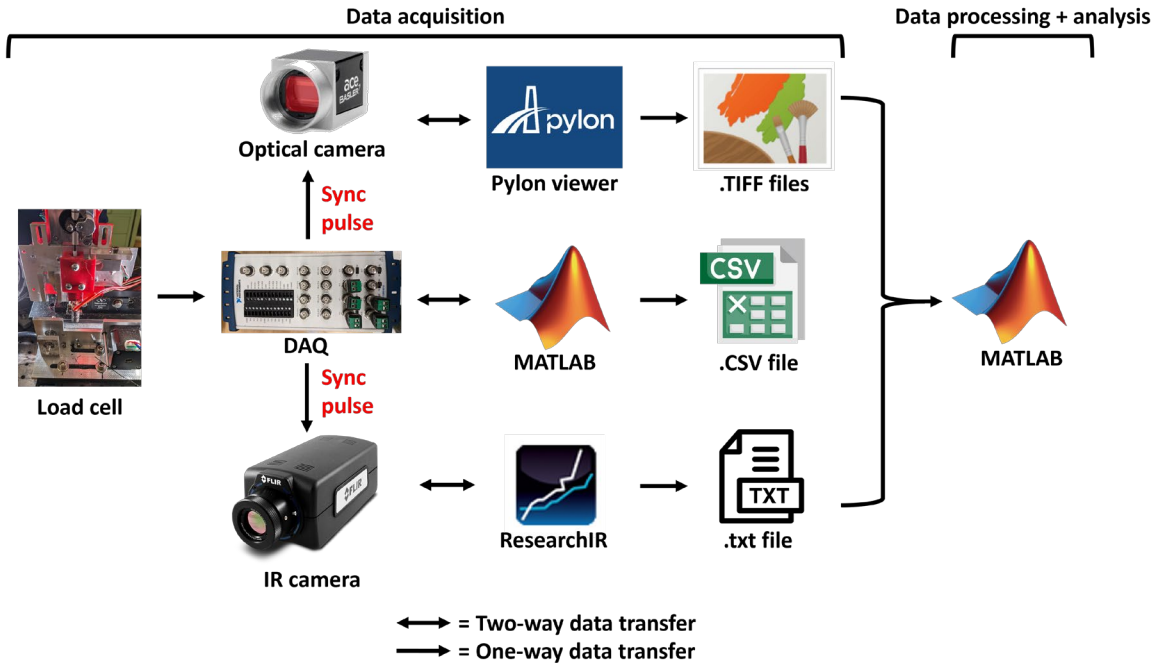

Figure 5: The flow of data from the sensors through analysis.

At the conclusion of data acquisition, all raw data is saved. Pylon Viewer outputs the optical images in the form of tag image file format (TIFF) files, MATLAB outputs the analog signals and timestamps in the form of comma-separated value (CSV) files, and ResearchIR initially saves the data as advanced extract, transform, load transformation script (ATS) files. TIFF and CVS file formats are readable by MATLAB for data processing. However, ATS files are not, so the data at a cursor on images in ResearchIR are exported as text (txt) files prior to processing and analysis in MATLAB. Example optical and IR images are shown in Figure 6. On the optical image, the double-sided red arrow represents an extrusion width measurement. The cursor on the extrudate of the IR image indicates the location of exported temperature values. The scale for the IR data is typically in 'counts', which represent the intensity of IR radiation. For ease of understanding, those IR counts have been converted into temperature values. To ensure data stream synchronization, the clock for each camera is synchronized with the clock on the computer. All three data streams record timestamps to the nearest second at a minimum, and

all image frames are numbered in order of collection. Synchronization is verified at the end of collection for each condition.

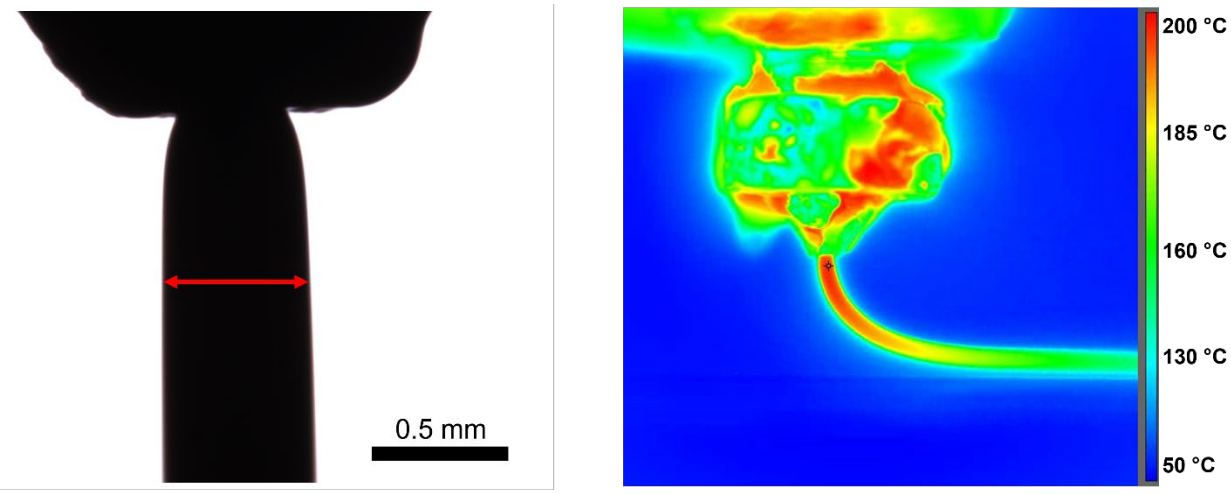

Figure 6: Example raw optical (left) and IR images (right).

Extrudate width is measured multiple times during each extrusion trial from optical images in the extrudate section where the width appears fully developed. Measurements are performed using a MATLAB script where the user defines the fully developed width region manually, then the image is turned to grayscale and binarized using functions from MATLAB's image processing toolbox, and the width is determined by the transitions in color. To account for curvature in the extrudate, measurements are taken straight across a row of pixels and at an angle up and down the extrudate from a fixed pixel on the left side of the extrudate. The Pythagorean theorem is used to determine the length of the lines measured at an angle. For measurements going up and down the extrudate, the minimum value is selected for each direction. Once all three width values are determined, the minimum is selected from the three to represent the extrudate width. This process is repeated for each pixel down the length of the extrudate within

the fully developed region for every image and condition. The extrudate width values for each image are saved to a MATLAB (MAT) file for each condition.

For the IR images, the average temperature value across the three-by-three pixel-sized cursor is exported as a function of time as a series of txt files. The .txt files are then imported into MATLAB, where stable measurement regions are identified, and the indices are saved for later analysis. A stable measurement region is typically at least two seconds long, to ensure an adequate number of measurements were used to calculate statistics later.

2.4. Calibration techniques

To ensure the correct flow rates are achieved by the printer, the stepper motor was calibrated by driving 100 mm lengths of filament into the hot end by the stepper motor with a mark that indicated 100 mm from the start of the PTFE tube. After extrusion, the length between the top of the PTFE tube and the mark was measured and the steps per millimeter value was updated for the extruder stepper motor in the controller interface on the Creality motherboard. A similar approach was taken for calibrating the steps per millimeter for the conveyor belt, by placing a piece of tape on the belt at one side of the nylatron platform and indexing the motor to position the conveyor the known length of the platform. With these systems calibrated, the test cell can simulate the printing process.

To calibrate the optical camera, images of a microscope slide with a one-millimeter-wide marking and 0.01 mm dividing marks were used. Five measurements were taken of 0.50 mm of the slide, yielding a calibration scale value of 0.0015 mm/pixel for the 4x zoom on the objective. The pixel width measurements recorded during processing were converted to millimeters using this scale immediately after measurement.

To calibrate the IR camera, a similar procedure was followed as in previous work from one of the authors [51]. The counts from the IR camera were converted into their respective temperature values after the .txt file for each condition was imported to MATLAB via a function containing the constants for a modified form of Planck's equation, as discussed in the work by Seppala and Migler [51].

To calibrate the load cell, one end was fixed with a vise while known weights were placed on the free end. The measured voltage was recorded by MATLAB during this procedure. After completion, a linear model was fit to replicate the known weights as a function of voltage recorded by the DAQ. The linear model provides the gain used to convert the voltage from the load cell to force values, which are converted to pressure values by dividing the force by the cross-sectional area of the filament during data processing.

2.5. Experimental design

To study die-swell, three factors were varied: volumetric flow rate, hot end temperature setpoint, and nozzle orifice diameter. The volumetric flow rates were selected based on realistic print speeds that slicers offer users and were primarily studied using the 0.40 mm nozzle, since it is the most popular of the three sizes purchased. The investigated print speeds and resulting shear rates are shown in Table 3; some extreme conditions were not investigated due to excessive pressures or melting requirements. The apparent shear rate at the wall was calculated according to equation (4) and the Power-law correct shear rate was calculated by equation (3), which corrects equation (4) for shear thinning. The hot end temperature setpoints of 200 °C, 225 °C, and 250 °C were selected to bracket the recommended processing temperature range of the ABS filament and provide a center point.

Table 3: Print speeds and the calculated volumetric flow rates, shear rates, and corrected shear rates used in the experiment

Nozzle orifice diameter [mm]		**0.25**	**0.4**	**0.6**	**0.25**	**0.4**	**0.6**
Print speed [mm/s]	**Volumetric flow rate [mm^3/s]**	**Apparent shear rate at wall, $\dot{\gamma}_{aw}$ [s^{-1}]**			**Power-law corrected shear rate, $\dot{\gamma}_w$ [s^{-1}]**		
10	0.9	600	140	N/A	900	200	N/A
30	2.5	1600	400	100	2500	600	200
55	5.0	3300	800	N/A	4900	1200	N/A
80	7.0	4600	1100	300	6900	1700	500
110	10.0	6500	1600	500	9800	2400	700

Each condition described in the experimental matrix was investigated by extruding for one minute and recording infeed pressure, measured temperature, and optical image data during that time. Since transient data was collected, each condition was executed once. If a significant error occurred while starting data acquisition and saving the data, the condition was repeated. Overall, thirty-three conditions are presented in this work and listed in Supplemental Table S.1 with different combinations of nozzle orifice diameter, hot end temperature setpoint, and volumetric flow rate.

2.6. Analysis

For the temperature and infeed pressure data, averages and standard deviations were calculated for each of the stable regions identified during data processing; these values are reported in the Results section. For each image, the extrudate width values are averaged across the length of the fully developed region. With the extrudate width value available, the swell ratio is calculated as follows:

$$S = W_E/D_N \quad (9)$$

where S is the swell ratio, W_E is the extrudate width, and D_N is the nozzle orifice diameter. For each condition, the average and standard deviation were calculated (across multiple images) and are presented in the results.

For the given experimental conditions, the shear stress in the nozzle orifice was calculated using the Cross-WLF model coefficients in Table 1, the Weissenberg-Rabinowitsch-corrected shear rate, and Newton's law of viscosity. This allows for analysis of die-swell as a function of shear stress. To model the swell ratio as a function of shear stress, Tanner's [16] model was adopted, which states the die-swell can be estimated as:

$$S = \left\{2 \int_0^1 [1 + (N_1/2\tau)^2 \,] \, \xi d\xi \right\}^{1/6} \quad (10)$$

where N_1 is the first normal stress difference and ξ is two times the radial coordinate divided by the diameter of the tube that the polymer is flowing through, τ is the shear stress. When evaluated at the wall of the tube, equation 10 arrives at the solution of:

$$S = (1 + f^2/2)^{1/6} \quad (11)$$

where f is equal to $N_1/2\tau$. Based on the work of Philippoff and Stratton [62] and Middleman [63], Tanner assumed f to be proportional to the shear stress multiplied by a constant, k_{N_1}, such that:

$$f \approx k_{N_1}\tau \quad (12)$$

Knowing the observed swell ratio and the modeled shear stress, τ, equation 12 is substituted into equation 11 and a model is fit in MATLAB, using fitnlm(), to find a value for k_{N_1}. The model is fit to data for all nozzle orifice diameters for each hot end temperature setpoint. This work assumes that k_{N_1} is constant for all nozzle orifice diameters but varies as a function of temperature. The validity of this assumption is assessed in the Results section.

3. Results and discussion

Infeed pressure as a function of volumetric flow rate is shown in Figure 7. The left subplot shows the infeed pressure as a function of volumetric flow rate for different hot end temperature setpoints for the 0.40 mm nozzle orifice diameter. The 0.40 mm nozzle was selected for this plot since it is the most popular size for thermoplastic material extrusion printers. There is a general trend of increasing infeed pressure with volumetric flow rate and melt viscosity. Also, the 200 °C series shows an 8.34 MPa change from the 0.9 mm^3/s to 10.0 mm^3/s and the 250 °C series shows a 2.47 MPa change, indicating that volumetric flow rate has a greater effect on infeed pressure at lower hot end temperature setpoints. The 200 °C hot end temperature setpoint at 10 mm^3/s shows the greatest infeed pressure, with a value of 10.94 MPa. The 250 °C hot end temperature setpoint at 0.9 mm^3/s shows the lowest infeed pressure, with a value of 1.15 MPa. For 10 mm^3/s, the highest flow rate, a decrease in infeed pressure is observed as a function of hot end temperature setpoint, with the infeed pressure decreasing from 10.94 MPa to 3.62 MPa. These results are consistent with processing theory given the decrease of melt viscosity with increased melt temperature.

The right subplot of Figure 7 shows infeed pressure as a function of volumetric flow rate for different nozzle orifice diameters at a hot end temperature setpoint of 200 °C. The data is displayed for 200 °C because the pressure is expected to be greatest at 200 °C based on the previous plot. These data series again show the general trend of increasing infeed pressure with volumetric flow rate. The 0.40 mm nozzle displayed the lowest infeed pressure, with a value of 2.60 MPa at 0.9 mm^3/s, and the highest infeed pressure, with a value of 10.94 MPa at 10 mm^3/s. At 2.5 mm^3/s, the 0.60 mm nozzle provides the lowest infeed pressure, with a value of 4.46 MPa, and the 0.25 mm nozzle provides the greatest infeed pressure, with a value of 7.17 MPa. This result shows that infeed pressure decreases as a function of the nozzle orifice diameter, which is

consistent with processing theory that indicates the flow resistance increases with decreasing bore diameter.

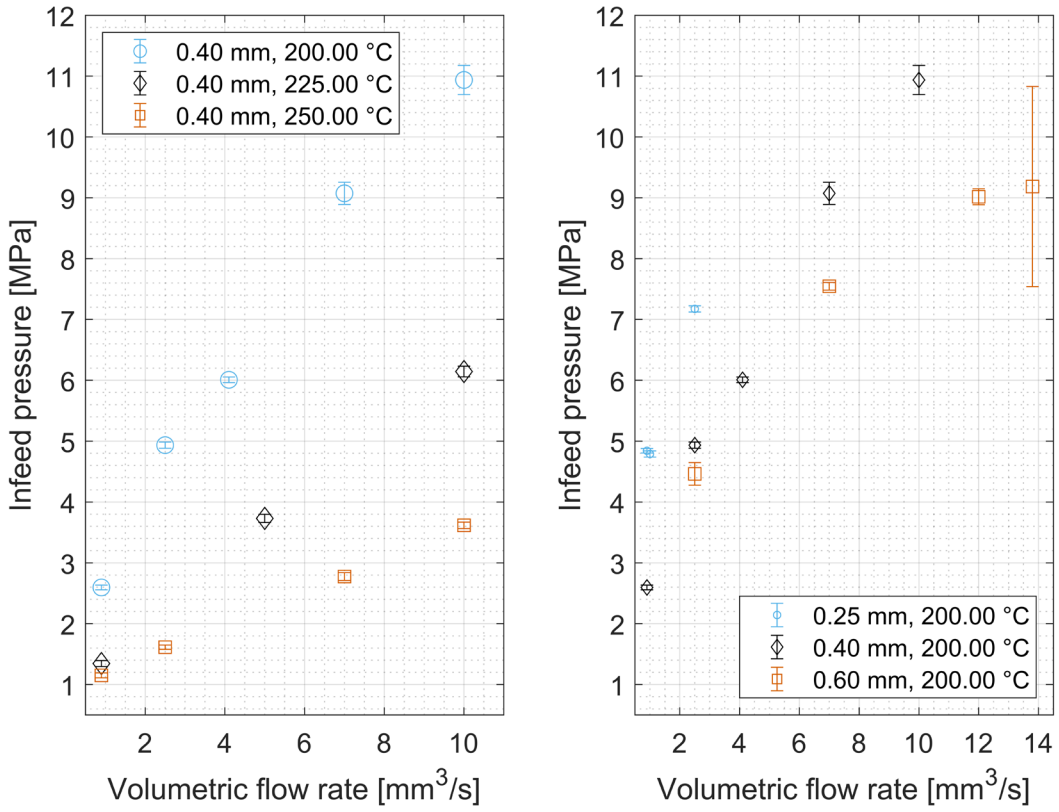

Figure 7: Infeed pressure versus volumetric flow rate for the 0.40 mm nozzle orifice diameter at different hot end temperature setpoints (left) and infeed pressure versus volumetric flow rate for different nozzle orifice diameters at a hot end temperature setpoint of 200 °C (right). The error bars represent one standard deviation of the infeed pressure.

Figure 8 shows the measured temperature as a function of the volumetric flow rate. The series in the lefthand subplot represent different hot end temperature setpoints for the 0.40 mm nozzle orifice diameter. The dashed lines represent the hot end temperature setpoint's nominal value for each series. The general trend shows the measured temperature is below the setpoint at the 0.9 mm^3/s, increases towards the set point around 2.5 mm^3/s and then decreases when the

flow rate increases to 10 mm^3/s. At a hot end temperature setpoint of 250 °C and volumetric flow rate 10 mm^3/s, the measured temperature deviated the most from its setpoint value with a measured value of 244.1 °C (a deviation of 5.9 °C). Then, at a hot end temperature setpoint of 200 °C, and a volumetric flow rate of 10 mm^3/s, the measured temperature deviates the least from its setpoint with a value of 199.8 °C (a difference of 0.2 °C). At a volumetric flow rate of 10 mm^3/s, the deviation from the setpoint increases as a function of the hot end temperature setpoint value.

The righthand subplot in Figure 8 displays measured temperature as a function of volumetric flow rate for the three different nozzle orifice diameters for the 200 °C hot end temperature setpoint. Different behaviors are observed for each of the nozzle orifice diameters. The 0.25 mm nozzle undershoots the hot end temperature setpoint, the 0.40 mm nozzle data points fall around the hot end temperature setpoint, and the 0.60 mm nozzle orifice diameter data points overshoot the hot end temperature setpoint. The maximum measured temperature is 209.6 °C for the 0.60 mm nozzle orifice diameter at 13.8 mm^3/s and the minimum measured temperature is 193.3 °C for the 0.25 mm nozzle orifice diameter at 0.9 mm^3/s. The greatest deviation from the hot end temperature setpoint is for the 0.60 mm nozzle orifice diameter at 13.8 mm^3/s, with a value of 9.6 °C, and the minimum deviation was found again to be the 0.40 mm nozzle at 10 mm^3/s at 0.2 °C.

The 0.25 mm nozzle shows a sharp increase in the measured temperature from a value of 193.3 °C at 0.9 mm^3/s to 197.6 °C at 2.5 mm^3/s. This produces a decrease in the deviation from the hot end temperature setpoint as a function of the volumetric flow rate (around a 4.3 °C decrease). The trend for the 0.40 mm nozzle orifice diameter is the same as the trend in the lefthand plot, as it is the same data set. For the 0.60 mm nozzle orifice diameter, the overshoot

increases as a function of the volumetric flow rate, with the value of the measured temperature increasing from 206.6 °C to 209.6 °C between 2.5 mm^3/s and 13.8 mm^3/s (an increase of 3 °C). At the same volumetric flow rate of 2.5 mm^3/s, there is an increasing trend in the measured temperature value as a function of the nozzle orifice diameter where the 0.25 mm nozzle orifice diameter undershoots by 2.4 °C, the 0.40 mm nozzle orifice diameter is closest to the hot end temperature setpoint with a slight overshoot of 0.4 °C, and the 0.60 mm nozzle overshoots by around 6.6 °C. The difference between the 0.60 mm diameter nozzle's measured temperature and the 0.25 mm nozzle orifice diameter's measured temperature is around 9 °C. Temperature deviation is correlated to orifice diameter when the sign of the deviation is accounted for. The temperature increasing as a function of the volumetric flow rate for the 0.25 mm and 0.60 mm nozzle orifice diameters is attributed to a curvature effect in the IR thermography, which results in higher temperatures when the material swells to larger diameters. This effect is also why the 0.60 mm nozzle orifice diameter data overshoots the temperature setpoint, relative to the other two nozzle orifice diameters. This effect deserves further investigation in a separate study.

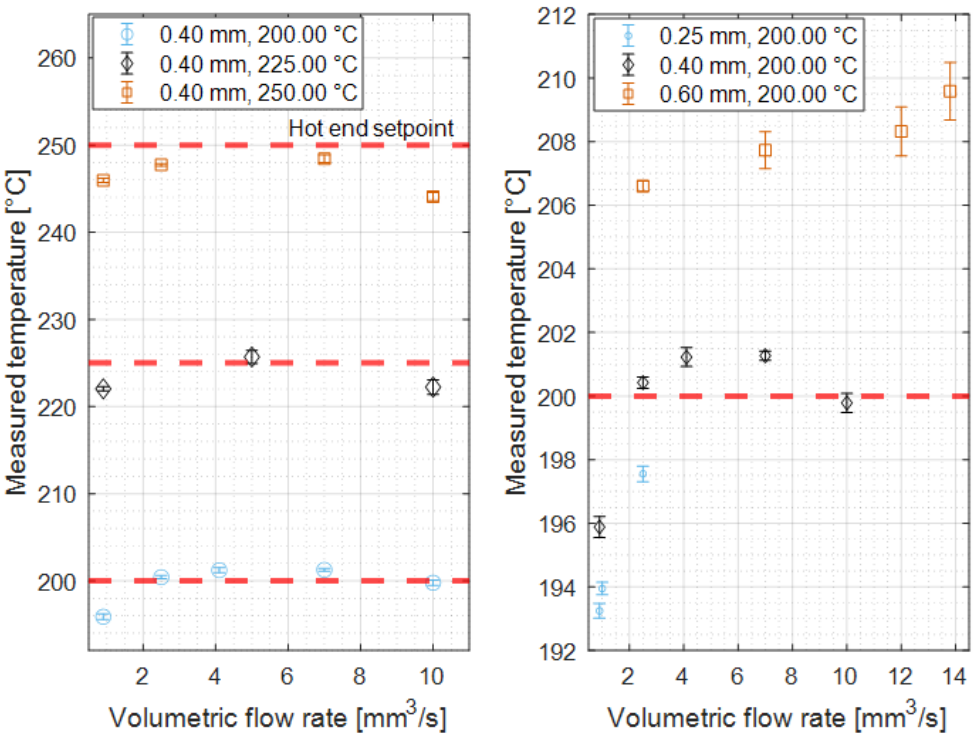

Figure 8: Measured temperature versus volumetric flow rate for varying hot end temperature setpoints with the 0.40 mm nozzle (left) and measured temperature versus volumetric flow rate for varying nozzle orifice diameters at a hot end temperature setpoint of 200 °C (right). The error bars represent one standard deviation of the measured temperature.

Figure 9 shows the swell ratio as a function of observed pressure and temperature for a 0.40 mm nozzle orifice diameter and a hot end temperature setpoint of 200 °C. The dashed lines indicate a swell ratio of 1.00, which will occur if the extrudate width is equal to the nozzle orifice diameter. For these plots, the volumetric flow rate is included in the legend to remind the reader of the effect of volumetric flow rate on the two responses.

The lefthand subplot shows swell ratio versus the infeed pressure. The minimum value for the swell ratio is 1.17, which means the extrudate width is 17 % greater than the nozzle orifice diameter. This value occurs at the minimum infeed pressure of 2.60 MPa (volumetric

flow rate of 0.9 mm^3/s). The maximum swell ratio is 1.45 and occurs at the maximum infeed pressure, 10.94 MPa (volumetric flow rate of 10 mm^3/s). The swell ratio appears proportional to the infeed pressure, with a slight curve in the trend. Die-swell is known to correlate with the shear stress the material is exposed to [18], and the infeed pressure and shear stress both increase as a function of the volumetric flow rate, causing this correlation.

The righthand subplot of Figure 9 shows the swell ratio as a function of measured temperature. For volumetric flow rates of 7 mm^3/s and below, swell ratio increases with increased temperature, appearing to follow either an exponential or power-law relationship. However, the 10 mm^3/s data point does not follow the same curve. These results highlight the effect of volumetric flow rate on the swell ratio, since the swell ratio continues to increase with volumetric flow rate, while the measured temperature decreases at the 10 mm^3/s volumetric flow rate. Shear stress is known to be a function of temperature for pseudoplastic fluids, since the viscosity is a function of temperature [61], so the swell ratio should correlate somewhat with the measured temperature. Still, the apparent trend between die-swell and temperature at higher volumetric flow rates was unexpected since it is unlikely that there is a direct relationship between the swell ratio and measured temperature. This unexpected behavior may be due to the extrudate width being measured during steady extrusion, which does not account for the width during periods of time when the material ceases to flow due to thermal gradients within the hot end. If the transient width were accounted for, the higher volumetric flow rates swell ratio would decrease and that data point would shift down and into the exponential trend. Based on these subplots, the average swell ratio shows a consistent correlation with the infeed pressure but does not appear to be a consistent function of the measured temperature.

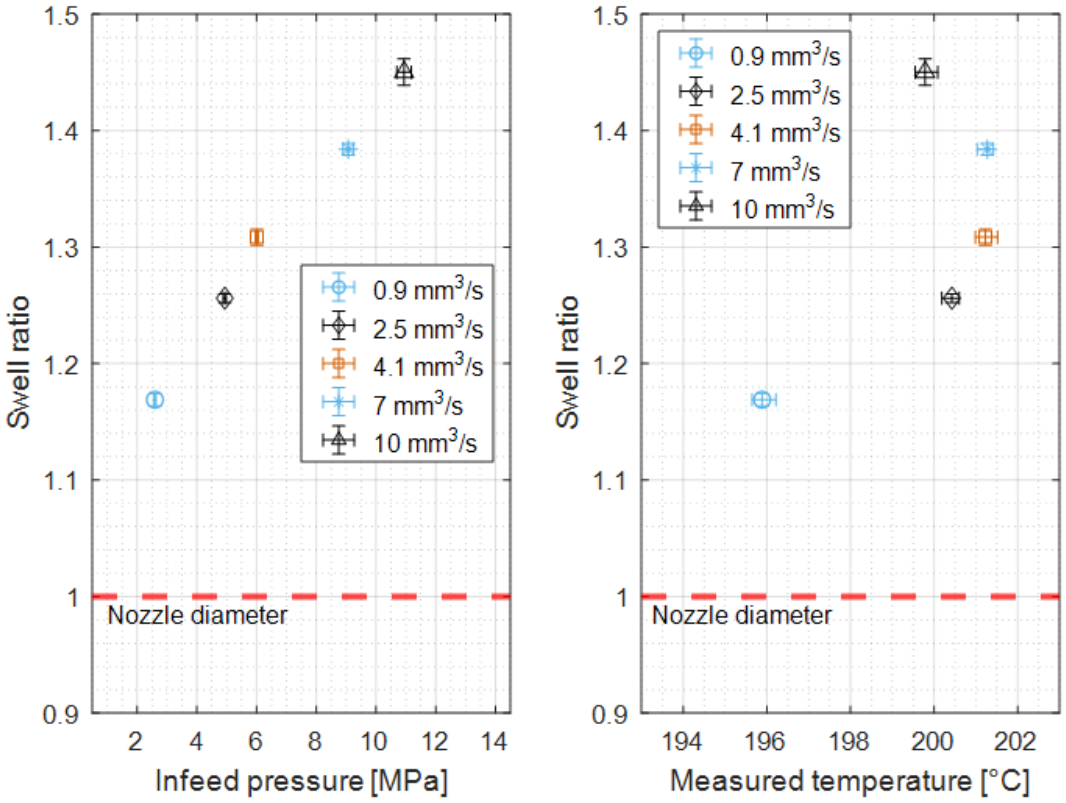

Figure 9: Swell ratio as a function of infeed pressure (left) and as a function of measured temperature (right) for the 0.40 mm nozzle orifice diameter at a hot end temperature setpoint of 200 °C. The error bars represent one standard deviation of the swell ratio for the y-axis and one standard deviation of the infeed pressure or measured temperature for the x-axis.

Figure 10 displays the effect of volumetric flow rate on swell ratio. The subplot on the left of Figure 10 includes a series of hot end temperature setpoints with a nozzle orifice diameter of 0.40 mm. In general, the swell ratio increases as a function of the volumetric flow rate. The minimum swell ratio is 1.12, for a volumetric flow rate of 0.9 mm^3/s and a hot end temperature setpoint of 250 °C, and the maximum swell ratio is 1.45, for a volumetric flow rate of 10 mm^3/s and a hot-end temperature setpoint of 200 °C; the range is 0.33. The 200 °C series has a minimum swell ratio of 1.17, a maximum of 1.45, and a range of 0.28. The 250 °C series has a

minimum of 1.12 and a maximum around 1.185, and a range of 0.065. Looking at the swell ratios for 10 mm^3/s, the swell ratio shows an inverse relationship with hot end temperature setpoint, with the greatest swell ratio, 1.45, being at the lowest hot end temperature setpoint, 200 °C, and the lowest swell ratio, 1.185, being at the highest hot end temperature setpoint, 250 °C; this results in a range of 0.265.

The righthand plot of Figure 10 shows swell ratios for different nozzle orifice diameters at a hot end temperature setpoint of 200 °C. On this plot, the swell ratio continues to increase as a function of the volumetric flow rate. The minimum swell ratio is 1.15, for the 0.60 mm nozzle at a volumetric flow rate of 2.5 mm^3/s, and the maximum swell ratio is 1.56, for the 0.25 mm nozzle orifice diameter with a volumetric flow rate of 2.5 mm^3/s; the range across all the data points on this plot is 0.41. Within the 0.25 mm nozzle orifice diameter data series, the swell ratio increases from 1.46 at a volumetric flow rate of 0.9 mm^3/s to 1.56 at a volumetric flow rate of 2.5 mm^3/s (a 0.10 range). For the 0.40 mm nozzle orifice diameter series, the swell ratio increases from 1.17 at a volumetric flow rate of 0.9 mm^3/s to 1.45 at a volumetric of 10 mm^3/s (a range of 0.28). Lastly, for the 0.60 mm nozzle orifice diameter series, the swell ratio increases from 1.15 at a volumetric flow rate of 2.5 mm^3/s to a value of 1.24 at a volumetric flow rate of 13.8 mm^3/s (a range of 0.09).

Die-swell experiments were performed with all nozzle orifice diameters at a volumetric flow rate of 2.5 mm^3/s. There is an inverse relationship between the nozzle orifice diameter and the swell ratio. The 0.60 mm nozzle orifice diameter has a swell ratio of 1.15 and the 0.25 mm nozzle orifice diameter has a swell ratio of 1.56, giving a range of 0.41, the greatest range for all three factors evaluated (followed by volumetric flow rate, then hot end temperature setpoint).

There is a clear relationship between the swell ratio and the set volumetric flow rate as shown in Figure 10. This behavior is driven by the greater shear stresses at higher volumetric flow rates. Similarly, in the lefthand plot, the decrease in the swell ratio as a function of the hot end temperature setpoint results from the shear stress decreasing with viscosity as a function of melt temperature. In the righthand figure, the trend of decreasing swell ratio as a function of the nozzle orifice diameter is also expected, since the material experiences a lower contraction ratio and lower shear stresses within the larger nozzle orifices.

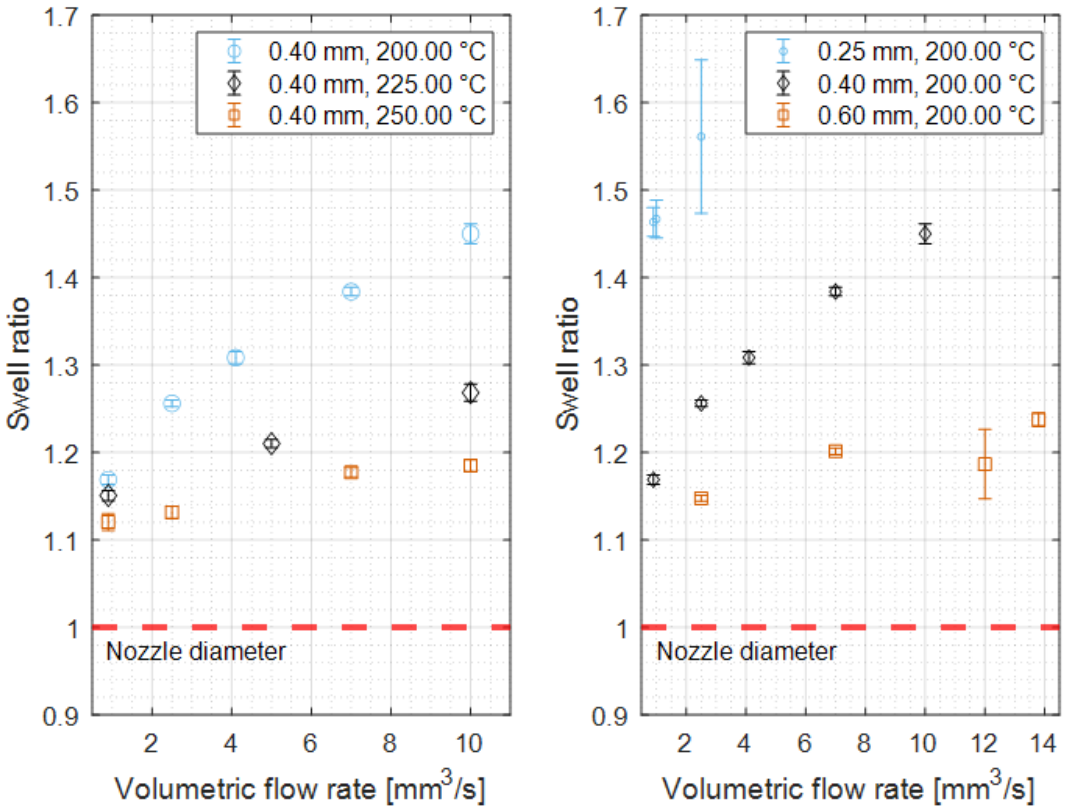

Figure 10: Swell ratio as a function of volumetric flow rate for the 0.40 mm nozzle orifice diameter at varying hot end temperature setpoints (left) and varying nozzle orifice diameters for a hot end temperature setpoint of 200 °C (right). The error bars represent one standard deviation of the swell ratio.

Figure 11 shows the swell ratio as a function of the shear stress at the wall in the nozzle orifice. Each of the plots contains the data for a different hot end temperature setpoint, with series of the different nozzle orifice diameters in each plot. It should be noted that, as the hot end temperature setpoint increases, higher volumetric flow rates are achievable with the 0.25 mm nozzle orifice diameter for a given maximum extruder force (melt pressure) constraint, so there are more data points for that nozzle orifice diameter in the 225 °C and 250 °C hot end temperature setpoint subplots than the 200 °C subplot. The coefficient of determination, R^2, values and estimates of k_{N_1} for the Tanner model are displayed on each plot.

Generally, the swell ratio is found to increase as a function of the shear stress in accordance with Tanner's model. In the lefthand plot of Figure 11, the swell ratio for the 200 °C hot end temperature setpoint is displayed for the different nozzle orifice diameters. The maximum swell ratio found for this temperature setpoint was for the 0.25 mm nozzle orifice diameter, with a value of 1.56 at a shear stress of 518 kPa. The minimum swell ratio was 1.15 for the 0.60 mm nozzle orifice diameter at a shear stress of 146 kPa, providing a range of 0.41 across the 200 °C data set. Within the 0.25 mm nozzle orifice diameter data set, the swell ratio ranged from 1.46 to 1.56 for shear stresses of 363 kPa and 518 kPa, respectively, and provided a range of 0.10. For the 0.40 mm nozzle, the swell ratio ranged from 1.17 to 1.45 at shear stresses of 157 kPa and 375 kPa, respectively, with a range of 0.28. The 0.60 mm nozzle orifice diameter swell ratios ranged from 1.15 to 1.24 for shear stresses of 146 kPa and 274 kPa, respectively, and provided a range of 0.09. There is a trend of decreasing range in swell ratio with increasing nozzle orifice diameter. The data fit well to the Tanner model with an R^2 value around 0.90.

The middle plot of Figure 11 provides the data set for the 225 °C hot end temperature setpoint. The swell ratio ranges from 1.11 for the 0.60 mm nozzle to 1.54 for the 0.25 mm nozzle

at shear stress values of 88 kPa and 430 kPa, respectively, providing a range of 0.43. Please note that the increased maximum shear stress relative to the 200 °C setpoint is due to the increased maximum volumetric flow rate being evaluated for the 0.25 mm nozzle orifice diameter relative to the lefthand plot. The R^2 for the Tanner model on this data is around 0.95, indicating higher model fidelity than the 200 °C data set. It should also be noted that the value for k_{N_1} increases from 1.02 x 10^{-5} Pa^{-1} to 1.12 x 10^{-5} Pa^{-1} as the hot end temperature setpoint increases, which is indicative of a greater proportion of melt elasticity, relative to the viscosity, at elevated temperatures.

The righthand plot of Figure 11 shows the different swell ratios for the 250 °C hot end temperature setpoint. The swell ratio varies from a minimum of 1.09 (for the 0.60 mm nozzle orifice diameter) to a maximum of 1.55 (for the 0.25 mm nozzle orifice diameter) for shear stresses of 115 kPa and 395 kPa, respectively. It should be noted that, on this plot, both the swell ratio and the standard deviation of the swell ratio decrease as a function of shear stress for the 0.60 mm nozzle orifice diameter. The R^2 value for the Tanner model on this data is around 0.94, indicating another good fit. Lastly, the value of k_{N_1} increases as a function of hot end temperature setpoint again, going from 1.12 x 10^{-5} Pa^{-1} for a hot end temperature setpoint of 225 °C to a value of 1.21 x 10^{-5} Pa^{-1} for a hot end temperature setpoint of 250 °C.

Figure 11 explicitly shows that die-swell is a function of the shear stress and that it can be predicted using the classic Tanner model. The die-swell increases as a function of shear stress as other researchers have observed [18, 25]. This figure also shows how shear stress decreases as a function of nozzle orifice diameter for the same volumetric flow rate and temperatures, leading to die-swell decreasing as a function of nozzle orifice diameter. The 200 °C data in the lefthand plot having the lowest R^2 value may be due to the deviations from the hot end temperature

setpoint value seen in Figure 8, which cause the shear stress and swell ratio to vary. Still, the goodness of fit across all three subplots shows that the assumption of k_{N_1} being constant for a material and independent of the nozzle geometry holds true. The value for k_{N_1} increasing as a function of temperature is due to shear stress decreasing as a function of increasing temperature.

The 0.60 mm nozzle orifice diameter swell ratio is observed to approach the swell ratio for a Newtonian fluid of approximately 1.12 as shown in Figure 11. This value of the Newtonian limit is discussed in the works of Tanner [16, 64] and other researchers [27, 31, 65], and has been experimentally observed [27, 65]. Alternative forms of Tanner's equation are available that account for this Newtonian value [16, 31, 64], but they affect the goodness of fit for viscoelastic materials [16]. The data for the 0.60 mm nozzle orifice diameter approaching the Newtonian fluid swell ratio value is an indicator of the material's viscosity and elasticity decreasing as a function of temperature, resulting in lower shear stresses.

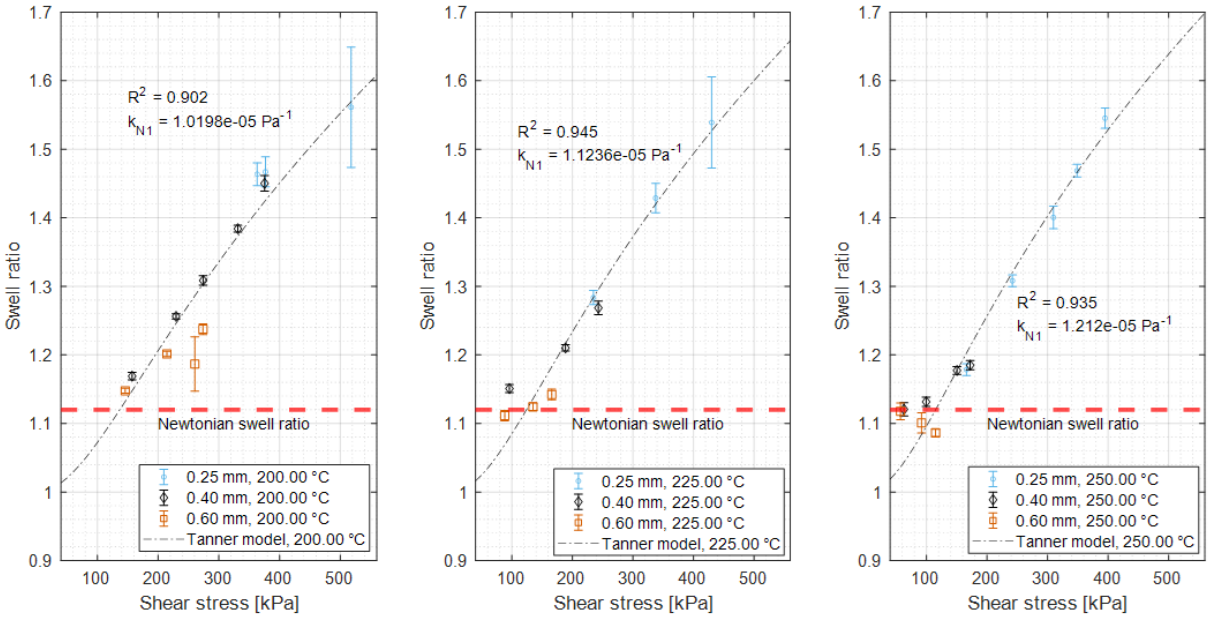

Figure 11: Swell ratio versus shear stress for various nozzle orifice diameters at a hot end temperature setpoint of 200 °C (left). Swell ratio versus shear stress for various nozzle orifice diameters at a hot end temperature setpoint of 225 °C (middle). Swell ratio versus shear stress for various nozzle orifice diameters at a hot end temperature setpoint of 250 °C (right). The dashed trendline on each plot represents the fitted Tanner model. The red, dashed, horizontal line at a swell ratio of 1.12 represents the swell ratio for a Newtonian fluid. The error bars represent one standard deviation of the swell ratio

Considering material rheology effects, there appears to be a strong relation between Tanner's constant, k_{N_1}, and the inverse of the zero-shear viscosity as a function of temperature. To make this relation more evident, Figure 12 shows these two variables as a function of temperature. In Figure 12, k_{N_1} is evaluated according to the statistical fits of the observed die-swell from Figure 11, while the inverse of the viscosity is evaluated according to the model of equation (2) with the fitted coefficients of Table 1, corresponding to the plotted viscosity values of Figure 2. The correlation coefficient between the two vectors of data (i.e., corrcoef(Kn,1/log10(eta_0)) in MATLAB) is 0.9990, indicating that there is a very high degree of correlation. Physically, this correlation is driven by the increase in the proportion of elastic behavior relative to viscous behavior as a function of temperature. To understand this relationship further, equation (12) was substituted into equation (11), Tanner's model. When solved for k_{N_1}, equation (13) is the result. Equation (13) shows that k_{N_1} is inversely proportional to the shear stress, which is a function of the zero-shear viscosity, resulting in the observed proportional relationship between the fit k_{N_1} values and the inverse of the zero-shear viscosity as a function of temperature. Accordingly, it is possible that die-swell effects may be well-estimated with rheological modeling of the materials being processed.

$$k_{N_1} = \sqrt{2(S^6 - 1)}/\tau \qquad [13]$$

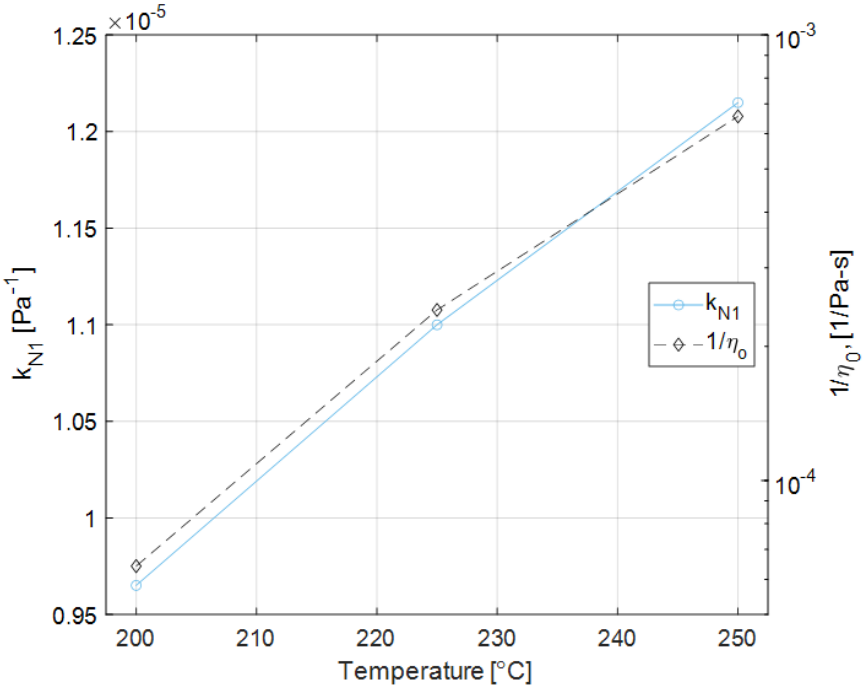

Figure 12. k_{N_1} and $1/\eta_0$ as a function of hot end temperature setpoint.

The results show that die-swell can cause the extrudate diameter to vary by 10 % to 60 % of the nozzle orifice diameter, and this effect is present even at steady state conditions. The fact that die-swell is shown to be a strong function of pressure, temperature, and flow rate suggests that transient control of the extrudate road may be improved by modeling die-swell.

4. Conclusions

The synchronization of infrared and optical cameras with an infeed pressure load cell has enabled the synchronous collection of extrudate width measurements, IR temperature measurements of the extrudate, and infeed force measurements. This data allows for calculation of the swell ratio, measured temperature, and infeed pressure for thermoplastic filaments, which can be used to characterize the material in-line, define processing windows, and provide insight into the material extrusion process.

The infeed pressure and measured temperature were shown to vary as a function of the volumetric flow rate, hot end temperature setpoint, and the selected nozzle orifice diameter. Additionally, the swell ratio was shown to vary as a function of the infeed pressure. The swell ratio was shown to be a function of the volumetric flow rate, hot end temperature setpoint, and the nozzle orifice diameter, with volumetric flow rate having the most significant effect. The swell ratio was also shown to vary as a function of shear stress, which was expected. The empirically fit Tanner model provides a good fit for this data set and shows that die-swell in material extrusion can be predicted using that relationship with the behavior strongly driven by the material rheology. Tanner's proportionality constant will vary as a function of temperature, yet the ABS studied approaches the Newtonian swell limit of 1.12 at lower flow rates and larger nozzle orifice diameters where the shear stress diminishes.

Supplemental materials

The full experimental matrix and a set of optical and IR images at each parameter level is provided in the supplemental materials binder. The MATLAB code used to generate the plots in the results and discussion sections is available upon request.

CRediT authorship contribution statement

Austin Colon: Conceptualization, Data curation, Formal analysis, Investigation, Methodology, Software, Validation, Visualization, Writing – original draft. **David Kazmer**: Conceptualization, Formal analysis, Funding acquisition, Investigation, Methodology, Project administration, Resources, Software, Supervision, Visualization, Writing – review & editing. **Jonathan Seppala**: Conceptualization, Formal analysis, Investigation, Methodology, Resources, Supervision, Writing – review & editing. **Amy Peterson**: Conceptualization, Funding acquisition, Investigation, Methodology, Project administration, Resources, Supervision, Writing – review & editing.

Declaration of competing interest

The authors declare no competing interests. One of the authors of this article is part of the Editorial Board of the journal. To avoid potential conflicts of interest, the responsibility for the editorial and peer-review process of this article lies with the journal's other editors. Furthermore, the authors of this article were removed from the peer review process and had no, and will not have, any access to confidential information related to the editorial process of this article.

Acknowledgements

This work is partially supported by the National Science Foundation (NSF) under GOALI Grant No. #1914651. Any opinions, findings, and conclusions or recommendations expressed in this material are those of the author(s) and do not necessarily reflect the views of the NSF. The authors would like to recognize the NSF INTERN supplement that was provided to the GOALI grant to support the first author's time at the National Institute of Standards of Technology (NIST). The authors also acknowledge Stratasys, Ltd. as the University of Massachusetts (UMass) Lowell team's GOALI partner. The first author would like to acknowledge NIST as well for agreeing to collaborate on these research efforts and supporting the first author's academic and professional development. More specifically, the first author recognizes the Polymers Processing Group and the Polymer Additive Manufacturing & Rheology Project at NIST for providing a wealth of knowledge, constructive criticism, and support. Lastly, the first author thanks the technicians at UMass Lowell and NIST that made instrumentation possible, David Rondeau and Christopher Amigo.

Data Availability

Data and implemented analyses are provided in the supplementary information.

References

[1] S.-I. Park and D. W. Rosen, Quantifying effects of material extrusion additive manufacturing process on mechanical properties of lattice structures using as-fabricated voxel modeling, Additive Manufacturing 12 (2016) 265-273, http://doi.org/10.1016/j.addma.2016.05.006

[2] S. Singh, G. Singh, C. Prakash, and S. Ramakrishna, Current status and future directions of fused filament fabrication, Journal of Manufacturing Processes 55 (2020) 288-306, http://doi.org/10.1016/j.jmapro.2020.04.049

[3] M. Salmi, Additive manufacturing processes in medical applications, Materials 14 (1) (2021), Article 191, http://doi.org/10.3390/ma14010191

[4] A. M. Gohn, D. Brown, G. Mendis, S. Forster, N. Rudd, and M. Giles, Mold inserts for injection molding prototype applications fabricated via material extrusion additive

manufacturing, Additive Manufacturing 51 (2022), Article 102595, http://doi.org/10.1016/j.addma.2022.102595
[5] J. E. Seppala, S. Hoon Han, K. E. Hillgartner, C. S. Davis, and K. B. Migler, Weld formation during material extrusion additive manufacturing, Soft Matter 13 (38) (2017) 6761-6769, http://doi.org/10.1039/c7sm00950j
[6] A. M. Peterson and D. O. Kazmer, Predicting mechanical properties of material extrusion additive manufacturing-fabricated structures with limited information, Sci Rep 12 (2022), Article 14736, http://doi.org/10.1038/s41598-022-19053-3
[7] T. J. Coogan and D. O. Kazmer, Prediction of interlayer strength in material extrusion additive manufacturing, Additive Manufacturing 35 (2020), Article 101368, http://doi.org/10.1016/j.addma.2020.101368
[8] S. Spiller, F. Berto, and S. M. J. Razavi, Mechanical behavior of material extrusion additive manufactured components: an overview, Structural Integrity Procedia 41 (2022) 158-174, http://doi.org/10.1016/j.prostr.2022.05.018
[9] N. R. Madhu, H. Erfani, S. Jadoun, M. Amir, Y. Thiagarajan, and N. P. S. Chauhan, Fused deposition modelling approach using 3D printing and recycled industrial materials for a sustainable environment: a review, Int J Adv Manuf Technol 122 (2022) 2125-2138, http://doi.org/10.1007/s00170-022-10048-y
[10] N. Vidakis, M. Petousis, S. Grammatikos, V. Papadakis, A. Korlos, and N. Mountakis, High performance polycarbonate nanocomposites mechanically boosted with titanium carbide in material extrusion additive manufacturing, Nanomaterials 12 (2022), Article 1068, http://doi.org/10.3390/nano12071068
[11] J. Yan, E. Demirci, A. Ganesan, and A. Gleadall, Extrusion width critically affects fibre orientation in short fibre reinforced material extrusion additive manufacturing, Additive Manufacturing 49 (2022), Article 102496, http://doi.org/10.1016/j.addma.2021.102496
[12] E. L. Gilmer, D. Miller, C. A. Chatham, C. Zawaski, J. J. Fallon, A. Pekkanen, T. E. Long, C. B. Williams, and M. J. Bortner, Model analysis of feedstock behavior in fused filament fabrication: enabling rapid materials screening, Polymer 152 (2018) 51-61, http://doi.org/10.1016/j.polymer.2017.11.068
[13] E. Garcia Plaza, P. J. N. Lopez, M. A. C. Torija, and J. M. C. Munoz, Analysis of pla geometric properties processed by FFF additive manufacturing: effects of process parameters and plate-extruder precision motion, Polymers 11 (2019), Article 1581, http://doi.org/10.3390/polym11101581
[14] F. Tamburrino, S. Graziosi, and M. Bordegoni, The influence of slicing parameters on the multi-material adhesion mechanisms of FDM printed parts: an exploratory study, Virtual and Physical Prototyping 14 (4) (2019) 316-332, http://doi.org/10.1080/17452759.2019.1607758
[15] E. Mitsoulis, G. C. Georgiou, and Z. Kountouriotis, A study of various factors affecting Newtonian extrudate swell, Computers & Fluids 57 (2012) 195-207, http://doi.org/10.1016/j.compfluid.2011.12.019
[16] R. I. Tanner, A Theory of Die Swell, Journal of Polymer Science: Part A-2 8 (1970) 2067-2078, http://doi.org/10.1002/pol.1970.160081203
[17] A. Merrington, Flow of visco-elastic materials in capillaries, Nature 152 (1943) 663, http://doi.org/10.1038/152663a0
[18] F. Alzarzouri and F. Deri, Evaluation of die swell behavior during capillary extrusion of poly(lactic acid)/ high density polyethylene blend melts, Technium: Romanian Journal of

Applied Sciences and Technology 2 (3) (2020) 34-42, http://doi.org/10.47577/technium.v2i3.387
[19] H. W. Müllner, J. Eberhardsteiner, and W. Fidi, Rheological characterization of the die swell phenomenon of rubber compounds, Polymer Testing 26 (8) (2007) 1041-1048, http://doi.org/10.1016/j.polymertesting.2007.07.003
[20] D. Tang, F. H. Marchesini, L. Cardon, and D. R. D'Hooge, State of the-art for extrudate swell of molten polymers: from fundamental understanding at molecular scale toward optimal die design at final product scale, Macromolecular Materials and Engineering 305 (11) (2020), Article 2000340, http://doi.org/10.1002/mame.202000340
[21] J.-Z. Liang, Melt die-swell behavior of polyoxymethylene blended with ethylene-vinyl acetate copolymer and high-density polyethylene, Polymer Testing 68 (2018) 213-218, http://doi.org/10.1016/j.polymertesting.2018.04.011
[22] J.-C. Huang and K.-S. Leong, Shear viscosity, extensional viscosity, and die swell of polypropylene in capillary flow with pressure dependency, Journal of Applied Polymer Science 84 (6) (2002) 1269-1276, http://doi.org/10.1002/app.10466
[23] D. M. G. Freitas, A. D. B. Oliveira, A. M. Alves, S. N. Cavalcanti, P. Agrawal, and T. J. A. Mélo, Linear low-density polyethylene/high-density polyethylene blends: effect of high-density polyethylene content on die swell and flow instability, Journal of Applied Polymer Science 138 (9) (2020), Article 49910, http://doi.org/10.1002/app.49910
[24] S. Eggen and E. L. Hinrichsen, Swell and distortions of high-density polyethylene extruded through capillary dies, Polymer Engineering and Science 36 (3) (1996) 410-424, http://doi.org/10.1002/pen.10428
[25] J. Z. Liang, Effects of extrusion conditions on die-swell behavior of polypropylene/diatomite composite melts, Polymer Testing 27 (8) (2008) 936-940, http://doi.org/10.1016/j.polymertesting.2008.08.001
[26] N. Sombatsompop and R. Dangtangee, Effects of the actual diameters and diameter ratios of barrels and dies on the elastic swell and entrance pressure drop of natural rubber in capillary die flow, Journal of Applied Polymer Science 86 (7) (2002) 1762-1772, http://doi.org/10.1002/app.11212
[27] E. Ben-Sabar and B. Caswell, Heat transfer effects in die swell, Journal of Rheology 25 (5) (1981) 537-548, http://doi.org/10.1122/1.549628
[28] J. Vlachopoulos, M. Horie, and S. Lidorikis, An evaluation of expressions predicting die swell, Transactions of the Society of Rheology 16 (4) (1972) 669-685, http://doi.org/10.1122/1.549269
[29] S. H. Sadek and M. Yildiz, Modeling die swell of second-order fluids using smoothed particle hydrodynamics, Journal of Fluids Engineering 135 (5) (2013), Article 051103, http://doi.org/10.1115/1.4023645
[30] V. Ganvir, A. Lele, R. Thaokar, and B. P. Gautham, Prediction of extrudate swell in polymer melt extrusion using an Arbitrary Lagrangian Eulerian (ALE) based finite element method, Journal of Non-Newtonian Fluid Mechanics 156 (1-2) (2009) 21-28, http://doi.org/10.1016/j.jnnfm.2008.06.006
[31] M. E. Mackay, The importance of rheological behavior in the additive manufacturing technique material extrusion, Journal of Rheology 62 (6) (2018) 1549-1561, http://doi.org/10.1122/1.5037687
[32] A. Das, E. L. Gilmer, S. Biria, and M. J. Bortner, Importance of polymer rheology on material extrusion additive manufacturing: correlating process physics to print properties,

ACS Applied Polymer Materials 3 (3) (2021) 1218-1249, http://doi.org/10.1021/acsapm.0c01228
[33] D. O. Kazmer, A. R. Colon, A. M. Peterson, and S. K. Kim, Concurrent characterization of compressibility and viscosity in extrusion-based additive manufacturing of acrylonitrile butadiene styrene with fault diagnoses, Additive Manufacturing 46 (2021), Article 102106, http://doi.org/10.1016/j.addma.2021.102106
[34] S. K. Kim, D. O. Kazmer, A. R. Colon, T. J. Coogan, and A. M. Peterson, Non-Newtonian modeling of contact pressure in fused filament fabrication, Journal of Rheology 65 (1) (2021) 27-42, http://doi.org/10.1122/8.0000052
[35] B. P. Heller, D. E. Smith, and D. A. Jack, Effects of extrudate swell and nozzle geometry on fiber orientation in Fused Filament Fabrication nozzle flow, Additive Manufacturing 12 (2016) 252-264, http://doi.org/10.1016/j.addma.2016.06.005
[36] P. Geng, J. Zhao, W. Wu, W. Ye, Y. Wang, S. Wang, and S. Zhang, Effects of extrusion speed and printing speed on the 3D printing stability of extruded PEEK filament, Journal of Manufacturing Processes 37 (2019) 266-273, http://doi.org/10.1016/j.jmapro.2018.11.023
[37] M. P. Serdeczny, R. Comminal, D. B. Pedersen, and J. Spangenberg, Experimental and analytical study of the polymer melt flow through the hot-end in material extrusion additive manufacturing, Additive Manufacturing 32 (2020), Article 100997, http://doi.org/10.1016/j.addma.2019.100997
[38] A. M. Yousefi, B. Smucker, A. Naber, C. Wyrick, C. Shaw, K. Bennett, S. Szekely, C. Focke, and K. A. Wood, Controlling the extrudate swell in melt extrusion additive manufacturing of 3D scaffolds: a designed experiment, J Biomater Sci Polym Ed 29 (3) (2018) 195-216, http://doi.org/10.1080/09205063.2017.1409022
[39] D. Tang, F. H. Marchesini, L. Cardon, and D. R. D'hooge, Evaluating the exit pressure method for measurements of normal stress difference at high shear rates, Journal of Rheology 64 (3) (2020) 739-750, http://doi.org/10.1122/1.5145255
[40] T. J. Coogan and D. O. Kazmer, In-line rheological monitoring of fused deposition modeling, Journal of Rheology 63 (1) (2019) 141-155, http://doi.org/10.1122/1.5054648
[41] A. Oleff, B. Küster, M. Stonis, and L. Overmeyer, Process monitoring for material extrusion additive manufacturing: a state-of-the-art review, Progress in Additive Manufacturing 6 (4) (2021) 705-730, http://doi.org/10.1007/s40964-021-00192-4
[42] T. Van Waeleghem, F. H. Marchesini, L. Cardon, and D. R. D'Hooge, Melt exit flow modelling and experimental validation for fused filament fabrication: From Newtonian to non-Newtonian effects, Journal of Manufacturing Processes 77 (2022) 138-150, http://doi.org/10.1016/j.jmapro.2022.03.002
[43] M. Preissler, C. Zhang, M. Rosenberger, and G. Notni, Platform for 3D inline process control in additive manufacturing, Optical Measurement Systems for Industrial Inspection X 10329 (2017), Article 103290R, http://doi.org/10.1117/12.2270493
[44] J. Li, W. Quan, L.-K. Shark, and H. Laurence Brooks, A vision-based monitoring system for quality assessment of fused filament fabrication (FFF) 3D printing, 2022 the 5th International Conference on Image and Graphics Processing (ICIGP) (2022) 242-250, http://doi.org/10.1145/3512388.3512424
[45] Y. Hong, M. Mrinal, H. S. Phan, V. D. Tran, X. Liu, and C. Luo, In-situ observation of the extrusion processes of acrylonitrile butadiene styrene and polylactic acid for material

extrusion additive manufacturing, Additive Manufacturing 49 (2022), Article 102507, http://doi.org/10.1016/j.addma.2021.102507
[46] C. Liu, A. C. C. Law, D. Roberson, and Z. Kong, Image analysis-based closed loop quality control for additive manufacturing with fused filament fabrication, Journal of Manufacturing Systems 51 (2019) 75-86, http://doi.org/10.1016/j.jmsy.2019.04.002
[47] M. Sgrulletti, M. Bragaglia, S. Giarnetti, L. Paleari, and F. Nanni, Understanding the impact of fused filament fabrication conditions on the microstructure and tensile properties of polyamide 6 by thermal and optical live monitoring, Materials Today Communications 28 (2021), Article 102679, http://doi.org/10.1016/j.mtcomm.2021.102679
[48] M. Borish, J. N. Zalameda, and A. Mendioroz, A survey of thermal sensing application in additive manufacturing, Thermosense: Thermal Infrared Applications XLIII 11743 (2021), Article 117430A, http://doi.org/10.1117/12.2587059
[49] D. Ravoori, C. Lowery, H. Prajapati, and A. Jain, Experimental and theoretical investigation of heat transfer in platform bed during polymer extrusion based additive manufacturing, Polymer Testing 73 (2019) 439-446, http://doi.org/10.1016/j.polymertesting.2018.11.025
[50] D. Pollard, C. Ward, G. Herrmann, and J. Etches, Filament temperature dynamics in fused deposition modelling and outlook for control, Procedia Manufacturing 11 (2017) 536-544, http://doi.org/10.1016/j.promfg.2017.07.147
[51] J. E. Seppala and K. D. Migler, Infrared thermography of welding zones produced by polymer extrusion additive manufacturing, Additive Manufacturing 12 (2016) 71-76, http://doi.org/10.1016/j.addma.2016.06.007
[52] J. Zhang, B. Van Hooreweder, and E. Ferraris, T4F3: temperature for fused filament fabrication, Progress in Additive Manufacturing 7 (2022) 971-991, http://doi.org/10.1007/s40964-022-00271-0
[53] F. Li, Z.-H. Yu, H. Li, Z.-S. Yang, Q.-S. Kong, and J. Tang, Real-time monitoring of raster temperature distribution and width anomalies in fused filament fabrication process, Advances in Manufacturing 10 (2022) 571-582, http://doi.org/10.1007/s40436-021-00385-8
[54] E. Ferraris, J. Zhang, and B. Van Hooreweder, Thermography based in-process monitoring of fused filament fabrication of polymeric parts, CIRP Annals 68 (1) (2019) 213-216, http://doi.org/10.1016/j.cirp.2019.04.123
[55] A. Lepoivre, N. Boyard, A. Levy, and V. Sobotka, Methodology to assess interlayer quality in the material extrusion process: a temperature and adhesion prediction on a high performance polymer, Additive Manufacturing 60 (2022), Article 103167, http://doi.org/10.1016/j.addma.2022.103167
[56] A. A. Rashid and M. Koc, Fused filament fabrication process: a review of numerical simulation techniques, Polymers 13 (20) (2021), Article 3534, http://doi.org/10.3390/polym13203534
[57] Z. Wang and D. E. Smith, A fully coupled simulation of planar deposition flow and fiber orientation in polymer composites additive manufacturing, Materials 14 (10) (2021), Article 2596, http://doi.org/10.3390/ma14102596
[58] N. Shadvar, E. Foroozmehr, M. Badrossamay, I. Amouhadi, and A. S. Dindarloo, Computational analysis of the extrusion process of fused deposition modeling of

acrylonitrile-butadiene-styrene, International Journal of Material Forming 14 (2019) 121-131, http://doi.org/10.1007/s12289-019-01523-1
[59] D. Mezi, G. Ausias, Y. Grohens, and J. Férec, Numerical simulation and modeling of the die swell for fiber suspension flows, Journal of Non-Newtonian Fluid Mechanics 274 (2019), Article 104205, http://doi.org/10.1016/j.jnnfm.2019.104205
[60] A. M. Peterson, Review of acrylonitrile butadiene styrene in fused filament fabrication: A plastics engineering-focused perspective, Additive Manufacturing 27 (2019) 363-371, http://doi.org/10.1016/j.addma.2019.03.030
[61] T. Osswald and N. Rudolph, Generalized Newtonian Fluid Models, in Polymer Rheology - Fundamentals and Applications. Cincinnati, Ohio: Hanser Publications, 2014, 59-97.
[62] W. Philippoff and R. A. Stratton, Correlation of the Weissenberg Rheogoniometer with Other Methods, Transactions of the Society of Rheology 10 (2) (1966) 467-487, http://doi.org/10.1122/1.549060
[63] S. Middleman, in The Flow of High Polymers. New York, New York: John Wiley and Sons Interscience, 1968, 187.
[64] R. I. Tanner, A theory of die-swell revisited, Journal of Non-Newtonian Fluid Mechanics 129 (2) (2005) 85-87, http://doi.org/10.1016/j.jnnfm.2005.05.010
[65] S. Middleman and J. Gavis, Expansion and contraction of capillary jets of newtonian liquids, Physics of Fluids 4 (3) (1961) 355-359, http://doi.org/10.1063/1.1706332